Insights into negative differential resistance in MoS_2 Esaki diodes: A first-principles perspective

Adam V. Bruce, Shuanglong Liu, James N. Fry, and Hai-Ping Cheng[*]
Department of Physics, University of Florida, Gainesville, Florida 32611, USA

(Received 14 May 2020; revised 5 August 2020; accepted 13 August 2020; published 14 September 2020)

MoS_2 is a two-dimensional material with a band gap depending on the number of layers and tunable by an external electric field. The experimentally observed intralayer band-to-band tunneling and interlayer band-to-band tunneling in this material present an opportunity for new electronic applications in tunnel field-effect transistors. However, such a widely accepted concept has yet to be been supported by theoretical investigations based on first principles. In this paper, using density functional theory, in conjunction with nonequilibrium Green's function techniques and our electric field gating method, enabled by a large-scale computational approach, we study the relation between band alignment and transmission in planar and side-stack MoS_2 *p-i-n* junction configurations. We demonstrate the presence of negative differential resistance for both in-plane and interlayer current, a staple characteristic of tunnel diode junctions, and analyze the physical origin of such an effect. Electrostatic potentials, the van der Waals barrier, and a complex band analysis are also examined for a thorough understanding of Esaki diodes.

DOI: 10.1103/PhysRevB.102.115415

I. INTRODUCTION

Following the advent of the tunnel diode, new efforts emerged to identify candidate materials for such electronics. Discovered by Esaki, these devices are valued for their possible applications in nanoscale circuitry [1]. Among these benefits is their usage in tunnel field-effect transistors (TFETs), which can have a lower theoretical subthreshold swing than traditional metal-oxide-semiconductor field-effect transistors (MOSFETs). The novel interlayer properties of atomically thin heterostructures have made such configurations attractive for TFET operation. The advantage in heterojunction-based tunnel diodes is their difference in the band structure between layers. External bias allows for programmable band alignment between layers, yielding nonlinear characteristics in band alignment. In particular, graphene and transition-metal dichalcogenides (TMDs) have been valued for their suitable dimensionality and electronic structure [2–5]. One such TMD is MoS_2, having a direct band gap in a single-layer configuration [6].

Recent experiments have shown a highly tunable band gap in bilayer MoS_2 under an external electric field [7]. Experimentally, there are difficulties in constructing heterojunctions using two-dimensional (2D) TMDs as leads [8]. Semiempirical studies have observed the presence of band-to-band tunneling in a nanoribbon under strain [9]. In addition, studies finding negative differential resistance in tunnel diode MoS_2 systems are a fairly recent phenomenon, most being published within the past half decade [10,11]. Within these studies, there has yet to be a comparison between planar and interlayer transport properties. A first-principles-based investigation is necessary to fully understand the electronic processes and the effects of band-to-band tunneling in *p-i-n* configuration MoS_2 diodes. Before introducing our model for this study, we should mention that we previously have developed and applied first-principles methods to investigate field effects related to tunneling transistors [12,13]. A number of systems were studied, focusing on different aspects of physical processes. Some other groups have also performed first-principles investigations to understand the field effects in tunneling junctions [14–16]; however, this study is an attempt that provides an analysis of interlayer band-to-band tunneling in MoS_2 bilayer systems in addition to a full analysis of band-to-band tunneling in a planar monolayer junction. The two types of junctions are prepared to separately quantify in-plane and interlayer tunneling. The rest of the paper is organized as follows: Section II describes theoretical approaches, computational details, and our simulation models; Sec. III presents our major results; and Sec. IV concludes our investigations with a discussion of some important issues.

II. METHODS

All of our calculations used a first-principles approach. Transport calculations were performed using density functional theory [17,18], with nonequilibrium Green's functions (NEGF + DFT) techniques as implemented in TRANSIESTA [19,20], which accounts for core electrons via nonlocal, norm-conserving pseudopotentials [21,22]. The self-consistent field (SCF) approach yields the necessary Green's functions to employ the Caroli formula for electron transmission [23,24],

$$T(E) = \mathrm{Tr}[G^a \Gamma^R G^r \Gamma^L], \qquad (1)$$

where G^a and G^r are advanced and retarded Green's functions, respectively, and Γ^R and Γ^L represent the level broadening functions for the right and left leads, respectively. This expression for the transmission function allows us to obtain the

*hping@ufl.edu

 ©2020 American Physical Society

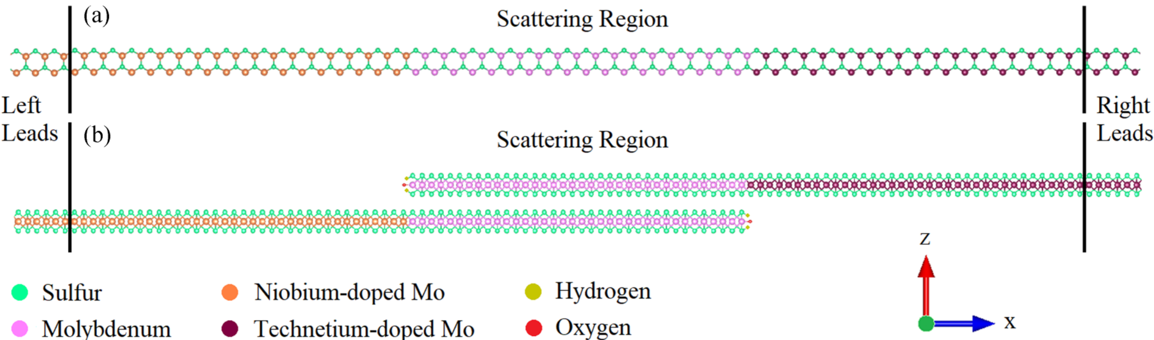

FIG. 1. Atomic structure of two molybdenum disulfide junctions (with H- and O-terminated edges). (a) is the top view of a *p-i-n* junction of single-layer MoS_2 consisting of 10% niobium- and technetium-doped leads; (b) is the side view of a *p-i-n* junction of overlapping, semi-infinite layers of MoS_2 with overlap in the undoped region. The vertical black lines mark the boundary of the scattering regions. For (b), the left electrode is connected to the lower layer while the right electrode is connected to the upper layer. Atomic positions are drawn with the VESTA visualization software [37].

current across the scattering region via the usual Landauer equation [25,26],

$$I = \frac{e}{h}\int_{\mu_R}^{\mu_L} dE[f_L(E) - f_R(E)]T(E), \tag{2}$$

where μ_L and μ_R are the chemical potentials of the left and right reservoirs, and f_L and f_R are Fermi functions in the left and right leads. For the basis set, we use a double-zeta plus polarization (DZP) basis. We also employ the Monkhorst-Pack method for sampling k points in the Brillouin zone [27]. Our rectangular supercell uses a $1 \times 11 \times 1$ grid for SCF calculations and a $1 \times 101 \times 1$ grid for all transmission calculations. We set the convergence requirement for the probability density matrix to 1×10^{-3}. Our functional for the exchange-correlation energy is within the generalized gradient approximation (GGA), specifically, the Perdew-Burke-Ernzerhof (PBE) form [18]. The applicability of this functional to our systems will be discussed in a later section.

In the experiments led by Chen, the metal leads were made by gating MoS_2 layers either positively or negatively [7]. In our simulation, we used doped leads, which are achieved by the virtual crystal approximation (VCA) as implemented in SIESTA. The VCA is a good approximation when the atomic number of the dopant atom is close to the atom it replaces, the doping concentration is relatively small, and wave functions spread over a large spatial region [28]. We use neighboring atoms on the periodic table in our doping scheme to comply with the former restriction and choose the two elements Nb and Tc to mimic hole-doped and electron-doped MoS_2, respectively. The very nature of the transport problem satisfies the latter. We apply this doping scheme to linearly shift the band structure of our leads, achieving the necessary nonequilibrium boundary conditions. However, the VCA cannot capture all the physics of random doping, which includes disordered scattering from random defects. Previous calculations show these effects on spin transport in nano-junctions [29]. Due to the nonlinear changes to conductance arising from these effects, it is unclear to what degree the VCA causes an overestimation or underestimation of transmission at this particular doping concentration compared to random doping. For the purposes of our study, we use the VCA to model gated leads rather than randomly doped leads.

We calculated the complex band structure of pristine monolayer and bilayer MoS_2 using the PWCOND part [30,31] of the QUANTUM ESPRESSO package [32,33]. During self-consistent calculations with QUANTUM ESPRESSO, we utilized the PBE exchange correlation energy functional [18] together with projector augmented-wave (PAW) pseudopotentials [34]. The pseudopotentials were generated using the PSLIBRARY package version 1.0.0 [35,36]. We applied 500 and 80 Ry energy cutoffs for expanding the charge density and the wave functions, respectively. The energy tolerance for self-consistency was set to 1×10^{-8} Ry. During complex band calculations with PWCOND, which is based on the self-consistent field previously found in QUANTUM ESPRESSO, we adopted an energy cutoff of 80 Ry for expanding the wave functions in two-dimensional planes as well. The number of subslabs was set to 30 to ensure high accuracy.

III. RESULTS

Figure 1(a) shows our monolayer structure that consists of a central pristine armchair MoS_2 ribbon of 18 unit cells in width (or length in the transport direction), bracketed by 18 niobium- (10%) or technetium-doped (10%) MoS_2 cells on each side and then by the two leads. The 18 unit cells right next to the pristine region or the scattering barrier serve as a buffer zone that screens charge accumulated next to the pristine region such that the whole scattering region is charge neutral. The pristine MoS_2 ribbon has a finite band gap thus functioning as the tunneling barrier. The left and right leads are also MoS_2 doped with 10% Nb and Tc, respectively, to create a *p-i-n* junction configuration. For this doping concentration, we performed a test for the screening length necessary for the transport calculation; we found that the size of the buffer zone is of adequate length to satisfy the charge neutrality condition and that the hopping parameters between the leftmost/rightmost unit cell in the buffer zone to the first unit cell of left/right lead is equal to the hopping between two adjacent unit cells in the left/right lead.

We analyzed the partial density of states (PDOS) according to

$$\mathrm{PDOS} = \frac{1}{\pi}\int d\mathbf{k}\, G^r[\Gamma_L + \Gamma_R]G^a, \tag{3}$$

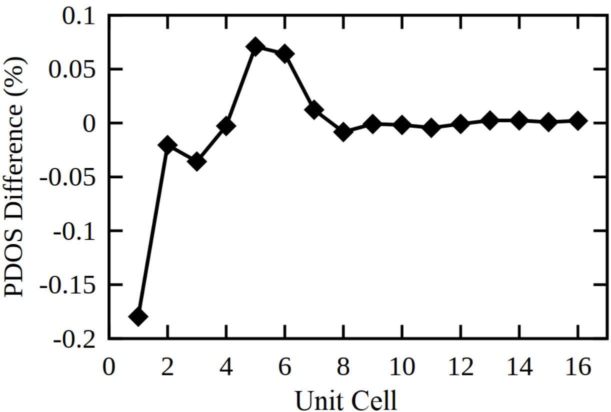

FIG. 2. Percent difference of the electrode and scattering region partial density of states. The difference is a function of the number of layers of unit cells from the pristine contact. This result shows the length of the doped contact in the scattering region necessary to approach bulklike PDOS.

in which the Green's function and level broadening functions are the same as those of the Caroli formula. A detailed comparison of the PDOS of our buffer zone or depletion region and electrode is illustrated in Fig. 2. Such a comparison is necessary considering the need for exact matching of the electronic density in the electrode and scattering region; this test indirectly verifies this agreement. It is clear that beyond 9 unit cells, the difference in the projected density of states between the buffer zone and a perfect lead is relatively small.

Figure 1(b) shows the configuration of our second junction. Compared to the planar configuration in Fig. 1(a), there is an overlapping region in the z direction that introduces a complexity in the junction and also allows interlayer electron tunneling. Again, the undoped insulating MoS_2 functions as the tunneling barrier. The configurations of the two junctions allow us to separately quantify in-plane and interlayer transport properties. Previous experimental studies have used similar configurations with heterojunctions and homojunctions to study the out-of-plane tunneling current [38,39]. Due to the

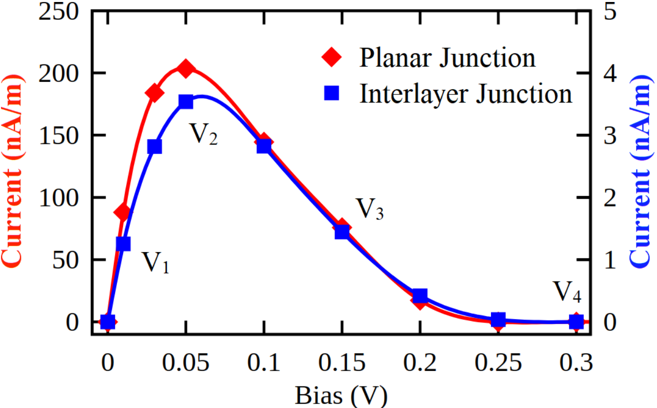

FIG. 3. The I-V curves for single-layer and overlap MoS_2 junctions, respectively. The scales for the two curves, left for the planar and right for the overlap, differ by a factor of 50. Both junctions show negative differential resistance.

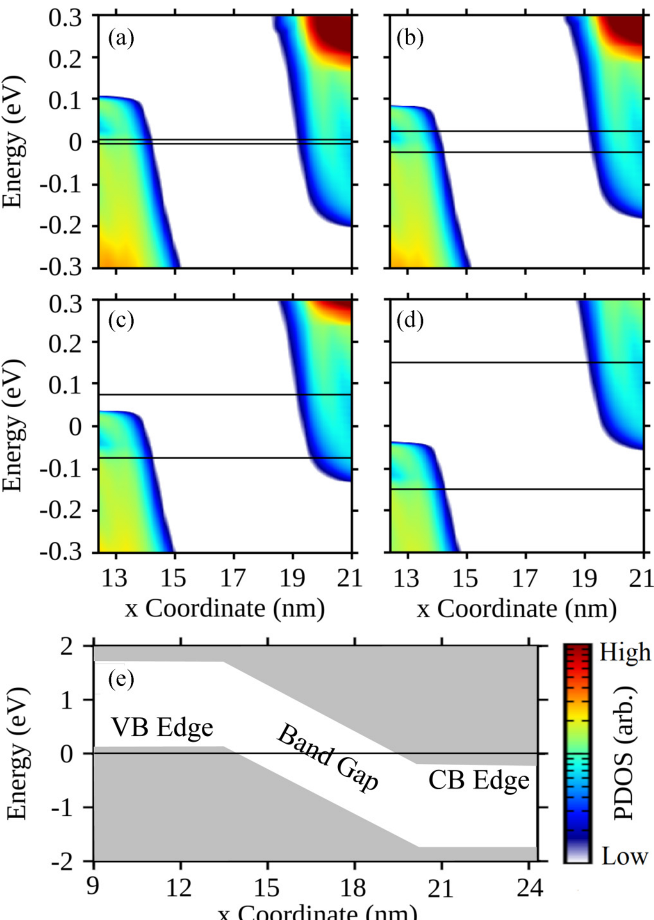

FIG. 4. (a)–(d) The partial density of states of the planar junction at biases V_1–V_4 in Fig. 3, respectively. The color bar shows the magnitude of the PDOS for (a)–(d) in logarithmic scale. (e) Band diagram at zero bias on a wider energy and position scale. VB and CB represent the valence band and conduction band, respectively.

sheared edge of the interlayer junction, hydrogen and oxygen serve as edge-terminating atoms. We will discuss edges and edge termination in a later section.

Figure 3 shows the calculated I-V curves of both the planar and the side-stacking or overlap junctions under low biases at room temperature. The characteristics of both graphs are similar, showing negative differential at biases higher than approximately 0.05 eV. Above roughly 0.25 eV, the current of both junctions drops by several orders of magnitude relative to the maximum current. These I-V curves are consistent with that of an Esaki diode in the forward-bias mode, containing a local maximum at low bias followed by a negative differential resistance regime [1]. The current in the planar junction reaches a maximum value roughly 50 times that for the junction of the side-stacking configuration, indicating the tunneling barrier across the two MoS_2 layers interacting by a van der Waals force is substantially higher than that across the 18 unit cells of MoS_2. Using a partial density of states analysis, we can evaluate the band character of the junctions at biases of interest.

Using the GGA functional, we calculated the band gap of monolayer MoS_2 to be 1.59 eV. This result differs from

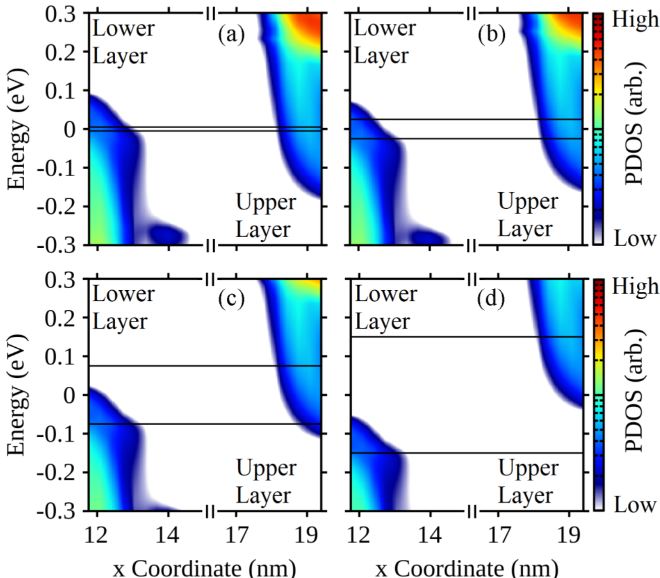

FIG. 5. (a)–(d) The density of states of the interlayer junction corresponding to biases V_1–V_4 in Fig. 3, respectively. The density across the junction is separated into lower and upper layers. Band alignment follows the same characteristics as that of the planar junction.

the measured value of greater than 1.9 eV [6]. With such a discrepancy, we expect an overestimation of tunneling current within our junctions. However, if the current arises from band to band tunneling effects, we do not expect the size of the band gap to impact the overall character of our *I-V* curve. This is due to band-to-band tunneling being driven by a relative band alignment. Additionally, the measured band gap of monolayer MoS_2 can vary as much as 1.39–2.16 eV due to environmental dielectric screening [40]. The discrepancy between measured and our calculated band gap is within this range of variations caused by environmental dielectric screening, which would be present in many electronic system. Thus, our calculated band gap could coincide with the measured band gap of monolayer MoS_2 in the presence of certain dielectrics. For these reasons, we believe that the GGA is sufficient for our calculations.

By plotting the PDOS of our planar junction at the biases of interest in Fig. 4 as a function of position along the transport direction and energy, we illuminate the transport properties of our systems. At V_1, the valence bands of the left electrode and the conduction bands of the right electrode are well aligned; however, the bias window is relatively small. The bands remain well aligned at V_2 with bias significantly increased. Further increases in bias skews the band alignment, as seen in V_3 and V_4, with alignment completely lost at the latter bias. Band-to-band tunneling can no longer contribute to current for biases greater than V_4. Band alignment within the bias window correlates with a higher current, characteristic of an Esaki diode.

In Fig. 5, we illustrate the PDOS as function of position and energy of the interlayer junction at the biases of interest. A comparison between PDOS and current indirectly shows intralayer and interlayer band-to-band tunneling across our junctions. Both planar and interlayer junctions share a similar

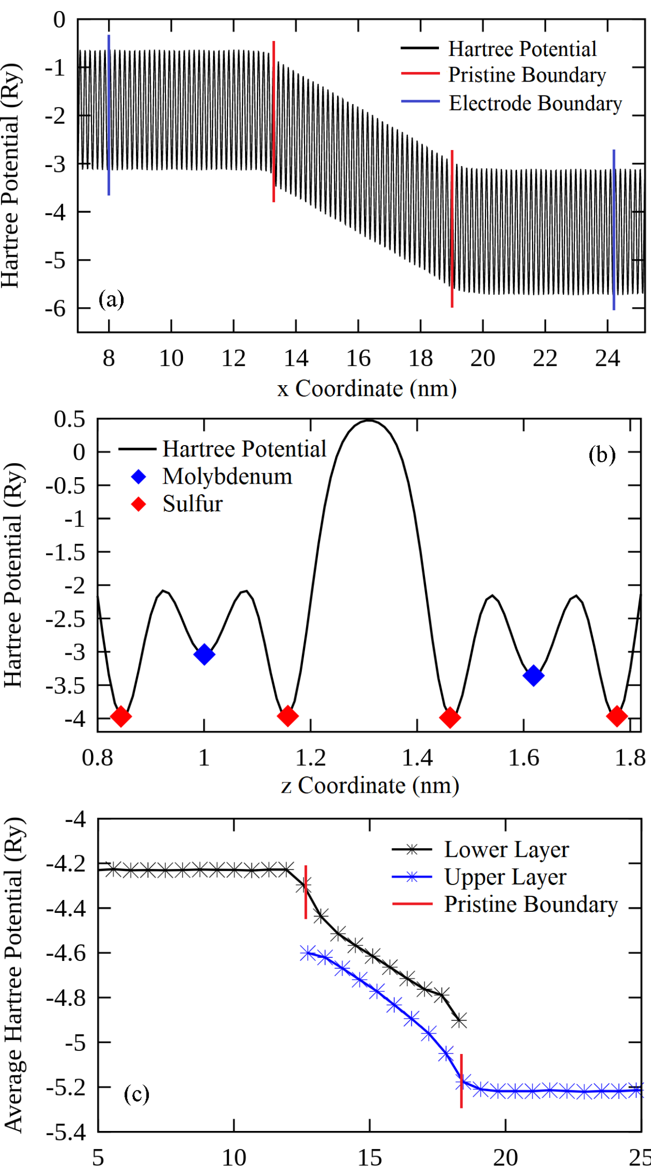

FIG. 6. The Hartree potential for both junctions. (a) The planar averaged Hartree potential of the planar junction as a function of *x* position. (b) The planar averaged Hartree potential of the interlayer junction as a function of *z* position. (c) The average Hartree potential for one unit cell of MoS_2 in the interlayer junction as a function of *x* position.

character in the density of states. However, the tunneling barriers are quite different. Figure 6 demonstrates this difference via the differing character of the Hartree potential between the junctions. The Hartree potential of the planar junction, seen in Fig. 6(a), can be plotted along the transport direction without discontinuity. As illustrated in Figs. 6(b) and 6(c), the interlayer junction has a potential barrier corresponding to the van der Waals gap. Figure 6(c) shows the relative difference in the Hartree potential between the two layers.

If band-to-band tunneling is the primary mechanism of transport across our junctions, we expect that transmission will coincide with the alignment of electrode bands. A comparison of both the electrode band structure and the

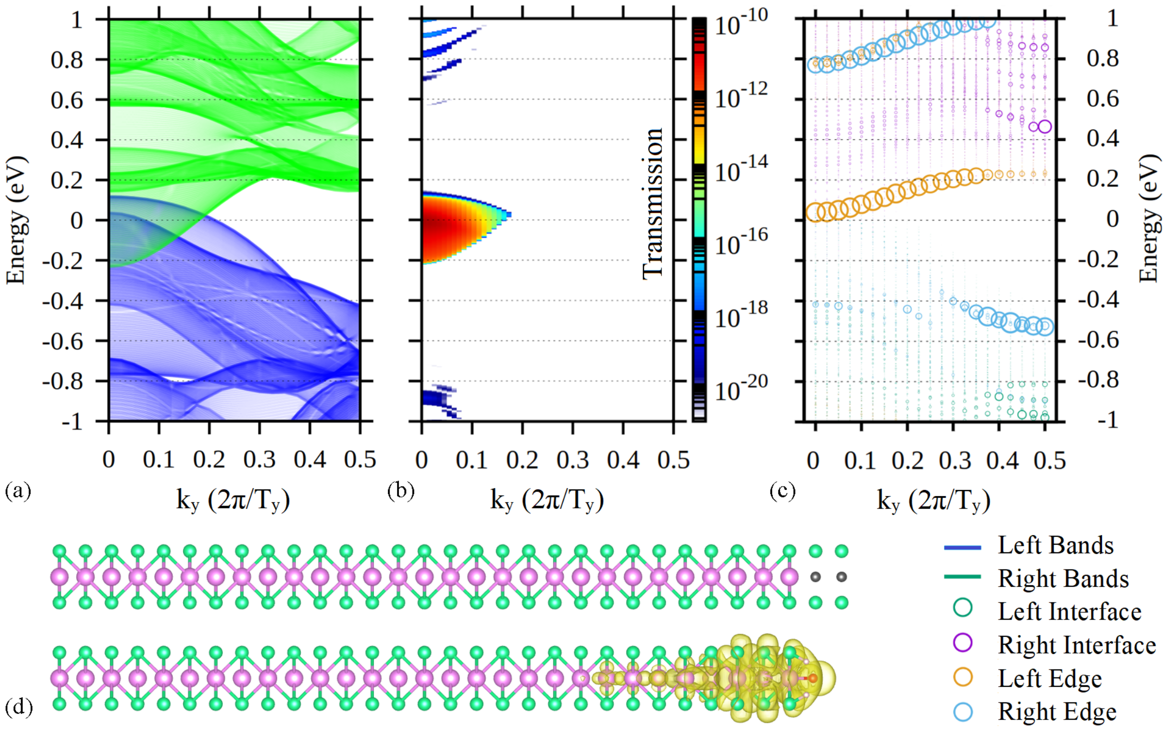

FIG. 7. (a) The valence band of the left electrode and the conduction band of the right electrode. (b) The transmission function of the interlayer junction at zero bias. A maximum transmission of 3.6×10^{-11} occurs at the gamma point at -7.5 meV. The overlap of the electrode bands coincides with the transmission of the junction. (c) Fat-band plots of the contribution to the local density of states of pristine MoS_2 unit cells: The fat bands of unit cells touching edge-terminating atoms and the fat bands of unit cells touching doped atoms. (d) The wave function corresponding to high LDOS near the Fermi energy seen in Fig. 5(c). The state is localized to the edge atoms.

transmission function is seen in Figs. 7(a) and 7(b). We see in the band structure of our electrodes an overlap around the Fermi energy; the broadest energy range of this overlap is at the Γ point in the first Brillouin zone. Alongside this band structure is the transmission function of the interlayer junction plotted in a logarithmic scaling. We illustrate the correlation of the electrode band crossing and transmission function by plotting both functions at the same energy and k path. Regions of highest band crossing coincide with the regions of highest transmission.

Previous studies show the effects of edge MoS_2 atoms on the electronic structure [41]. Charge accumulation on the edge atoms leads to a deviation from the bulk electron density. In order to mitigate these effects, we follow the edge-terminating structure of relaxing H and O onto bare MoS_2. We analyze the contribution to the local density of states (LDOS) of edge pristine MoS_2 unit cells via fat bands. These are compared to the LDOS of the unit cells adjacent to doped MoS_2 in Fig. 7(c). The edge unit cells show a high contribution to the density of states at the bottom of the conduction band. As these states fall within our bias window, we must ensure that edge states do not connect to the electrodes. In Fig. 7(d), we show the lowest-energy, conduction-band wave function of the lower-layer edge unit cell. This state corresponds to the highest local density of states near the Fermi energy on these edge atoms. We can see that the wave function does not connect to either electrode and is localized to the lower layer. Sampling other wave functions along the k path, we see that the states are likewise localized.

In order to understand the in-plane decay of the electron wave function into the intrinsic region of the two p-i-n junctions, we calculated the complex band structure of both monolayer and bilayer MoS_2. Figure 8(a) shows the complex band structure of monolayer MoS_2 to exhibit the evanescent states that decay in the transport direction of the planar junction. The reader may recall that the planar junction is in the x-y plane and electron transport is along the x direction. The wave vector k_y for the periodic y direction is set to zero here since the electron transmission at this point is highest at the Fermi energy. There are eight species of evanescent states at Fermi energy for $\mathrm{Im}\, k_x < 0.3(2\pi/T_x)$, in which T_x is the period of monolayer MoS_2 in the transport direction of the planar junction. Two of them consist of slowly decaying states near the top of the valence band or the bottom of the conduction band. They are marked as species I and II in Fig. 8(a). Hereafter, a valence top refers to a local maximum of the valence band under the constraint that k_y is zero, and similarly for a conduction bottom. This is for the convenience of describing the connectivity between complex bands and real bands. Species I derives from a valence top, and it is almost flat before $\mathrm{Im}\, k_x \sim 0.15(2\pi/T_x)$. The band flatness indicates that this species quickly becomes decaying states as the energy increases from the valence top. After $\mathrm{Im}\, k_x \sim 0.15(2\pi/T_x)$, species I splits into two, an upper part and a lower part, with the upper part connecting to an unoccupied band much higher above the conduction bottom. Species II connects a valence top and a conduction bottom, enclosing an area over the band gap. This area is minimal among all

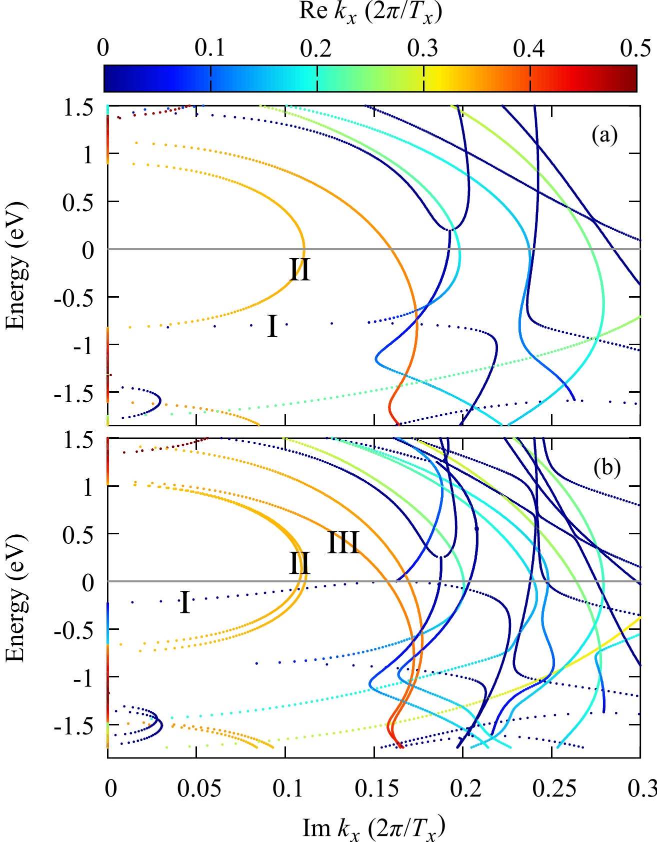

FIG. 8. Complex band structure for (a) monolayer and (b) bilayer MoS_2 as in the planar and the interlayer junctions, respectively. k_y equals zero for both (a) and (b). The Fermi level is set to zero and marked by a gray solid line.

areas that are enclosed by complex bands over the forbidden gap. Within the Wentzel-Kramers-Brillouin approximation, the band-to-band tunneling probability decays exponentially with such a minimum area [42,43].

Figure 8(b) shows the complex band structure of a bilayer MoS_2. In this case, there are three species of complex bands which consist of slowly decaying states around the valence top or the conduction bottom. They are marked again by species I, II, and III in Fig. 8(b). Species I of bilayer MoS_2 is similar to species I of monolayer MoS_2 in three aspects: (1) Both of them are derived from the top of a valence band; (2) a single band splits into two bands at $\mathrm{Im}\, k_x \sim 0.15(2\pi/T_x)$; and (3) $\mathrm{Re}\, k_x$ equals zero before the band splitting. Note that T_x of bilayer MoS_2 is the same as that of monolayer MoS_2. Species II of bilayer MoS_2 contains two copies of the domelike complex band, each of which resembles species II of monolayer MoS_2. Species III of bilayer MoS_2 is derived from the conduction bottom, and it extends into energies much lower than the valence top. For bilayer MoS_2, the minimum area of complex bands over the band gap is enclosed by both species I and II. When species I crosses species II, an electron may transit between the two species with the aid of phonons since the two species are different in crystal momentum $\mathrm{Re}\, k_x$ and momentum is conserved during the transition. Phonon-assisted scattering may reduce the electron transmission and thus degrades the performance of the relevant electronic device [44].

IV. CONCLUSION

We simulated armchair monolayer and interlayer MoS_2 *p-i-n* junctions consisting of doped MoS_2 leads. Simulations were performed using NEGF + DFT in order to account for nonequilibrium conditions in the leads. Both junctions showed an initial positive differential resistance followed by a transition to negative differential resistance past a current maximum. An analysis of the partial density of states at different biases revealed a band alignment consistent with Esaki diode behavior. Furthermore, the band structures of both leads intersected at the same energy and k points comprising the transmission of the interlayer junction. These results confirm band-to-band tunneling as the primary mechanism of charge transfer in the low-bias regime. Additionally, in-plane and interlayer band-to-band tunneling yields the same *I-V* curve character, differing only in magnitude. However, the two junctions significantly differ in Hartree potential, the interlayer junction having a large tunneling barrier in the van der Waals gap. The planar junction, being continuous in the transport direction, has no such electrostatic barrier. Our complex band analysis reveals the slowest decaying evanescent states that contribute the most to the band-to-band tunneling probability. Phonon-assisted electron tunneling is more likely to occur in the interlayer junction than in the planar junction, degrading the performance of electronic devices based on bilayer MoS_2.

Due to the known issues with edge termination in MoS_2 simulations, we used a H and O edge-terminating scheme. The local density of states, obtained via fat-band calculations, shows edge states near the Fermi energy. These states, however, are shown to have no effect on transport properties, as they are wholly localized to the edges of the interlayer junction.

ACKNOWLEDGMENTS

This work was supported by the US Department of Energy (DOE), Office of Basic Energy Sciences (BES), under Contract No. DE-FG02-02ER45995. Computations were done using the utilities of National Energy Research Scientific Computing Center and University of Florida Research Computing.

[1] L. Esaki, Phys. Rev. **109**, 603 (1958).

[2] L. Britnell, R. V. Gorbachev, R. Jalil, B. D. Belle, F. Schedin, A. Mishchenko, T. Georgiou, M. I. Katsnelson, L. Eaves, S. V. Morozov, N. M. R. Peres, J. Leist, A. K. Geim, K. S. Novoselov, and L. A. Ponomarenko, Science **335**, 947 (2012).

[3] Y.-P. Wang, J. N. Fry, and H.-P. Cheng, ACS Omega **2**, 5824 (2017).

[4] G.-X. Chen, X.-G. Li, Y.-P. Wang, J. N. Fry, and H.-P. Cheng, Phys. Rev. B **95**, 045302 (2017).
[5] B. Radisavljevic, A. Radenovic, J. Brivio, V. Giacometti, and A. Kis, Nat. Nanotechnol. **6**, 147 (2011).
[6] K. F. Mak, C. Lee, J. Hone, J. Shan, and T. F. Heinz, Phys. Rev. Lett. **105**, 136805 (2010).
[7] T. Chu, H. Ilatikhameneh, G. Klimeck, R. Rahman, and Z. Chen, Nano Lett. **15**, 8000 (2015).
[8] S. Kang, X. Mou, B. Fallahazad, N. Prasad, X. Wu, A. Valsaraj, H. C. P. Movva, K. Kim, E. Tutuc, L. F. Register, and S. K. Banerjee, J. Phys. D: Appl. Phys. **50**, 383002 (2017).
[9] R. K. Ghosh and S. Mahapatra, IEEE Trans. Electron Devices **60**, 274 (2013).
[10] A. Nourbakhsh, A. Zubair, M. S. Dresselhaus, and T. Palacios, Nano Lett. **16**, 1359 (2016).
[11] R. Zhang, C. An, L. Xu, S. Wu, D. Zhang, X. Hu, and J. Liu, ACS Appl. Electron. Mater. **1**, 523 (2019).
[12] S. Liu, Y. Xu, Y.-P. Wang, Y. P. Chen, J. N. Fry, and H.-P. Cheng, Appl. Phys. Lett. **116**, 031601 (2020).
[13] X.-G. Li, Y.-P. Wang, X. G. Zhang, and H.-P. Cheng, arXiv:1705.01205.
[14] M. H. Bani-Hashemian, S. Bruck, M. Luisier, and J. VandeVondele, J. Chem. Phys. **144**, 044113 (2016).
[15] T. Sohier, M. Calandra, and F. Mauri, Phys. Rev. B **96**, 075448 (2017).
[16] T. Brumme, M. Calandra, and F. Mauri, Phys. Rev. B **89**, 245406 (2014).
[17] W. Kohn and L. J. Sham, Phys. Rev. **140**, A1133 (1965).
[18] J. P. Perdew, K. Burke, and M. Ernzerhof, Phys. Rev. Lett. **77**, 3865 (1996).
[19] M. Brandbyge, J.-L. Mozos, P. Ordejón, J. Taylor, and K. Stokbro, Phys. Rev. B **65**, 165401 (2002).
[20] J. Taylor, H. Guo, and J. Wang, Phys. Rev. B **63**, 245407 (2001).
[21] J. M. Soler, E. Artacho, J. D. Gale, A. García, J. Junquera, P. Ordejón, and D. Sánchez-Portal, J. Phys.: Condens. Matter **14**, 2745 (2002).
[22] N. Troullier and J. L. Martins, Phys. Rev. B **43**, 1993 (1991).
[23] C. Caroli, R. Combescot, P. Nozieres, and D. Saint-James, J. Phys. C: Solid State Phys. **4**, 916 (1971).
[24] Y. Meir and N. S. Wingreen, Phys. Rev. Lett. **68**, 2512 (1992).
[25] R. Landauer, IBM J. Res. Dev. **1**, 223 (1957).
[26] R. Landauer, Philos. Mag. **21**, 863 (1970).
[27] H. J. Monkhorst and J. D. Pack, Phys. Rev. B **13**, 5188 (1976).
[28] R. J. Elliott, J. A. Krumhansl, and P. L. Leath, Rev. Mod. Phys. **46**, 465 (1974).
[29] J. Yan, S. Wang, K. Xia, and Y. Ke, Phys. Rev. B **97**, 014404 (2018).
[30] A. Smogunov, A. Dal Corso, and E. Tosatti, Phys. Rev. B **70**, 045417 (2004).
[31] H. J. Choi and J. Ihm, Phys. Rev. B **59**, 2267 (1999).
[32] P. Giannozzi, O. Andreussi, T. Brumme, O. Bunau, M. B. Nardelli, M. Calandra, R. Car, C. Cavazzoni, D. Ceresoli, M. Cococcioni, N. Colonna, I. Carnimeo, A. Dal Corso, S. de Gironcoli, P. Delugas, R. A. DiStasio, A. Ferretti, A. Floris, G. Fratesi, G. Fugallo *et al.*, J. Phys.: Condens. Matter **29**, 465901 (2017).
[33] P. Giannozzi, S. Baroni, N. Bonini, M. Calandra, R. Car, C. Cavazzoni, D. Ceresoli, G. L. Chiarotti, M. Cococcioni, I. Dabo, A. Dal Corso, S. de Gironcoli, S. Fabris, G. Fratesi, R. Gebauer, U. Gerstmann, C. Gougoussis, A. Kokalj, M. Lazzeri, L. Martin-Samos *et al.*, J. Phys.: Condens. Matter **21**, 395502 (2009).
[34] P. E. Blochl, Phys. Rev. B **50**, 17953 (1994).
[35] A. Dal Corso, Comput. Mater. Sci. **95**, 337 (2014).
[36] A. D. Corso, https://dalcorso.github.io/pslibrary/ (2013).
[37] K. Momma and F. Izumi, J. Appl. Crystallogr. **44**, 1272 (2011).
[38] S. Agarwal, J. T. Teherani, J. L. Hoyt, D. A. Antoniadis, and E. Yablonovitch, IEEE Trans. Electron Devices **61**, 1599 (2014).
[39] T. Roy, M. Tosun, X. Cao, H. Fang, D.-H. Lien, P. Zhao, Y.-Z. Chen, Y.-L. Chueh, J. Guo, and A. Javey, ACS Nano **9**, 2071 (2015).
[40] J. Ryou, Y.-S. Kim, S. KC, and K. Cho, Sci. Rep. **6**, 29184 (2016).
[41] L. Zhang, L. Wan, Y. Yu, B. Wang, F. Xu, Y. Wei, and Y. Zhao, J. Phys. Chem. C **119**, 22164 (2015).
[42] W. A. Harrison, Phys. Rev. **123**, 85 (1961).
[43] M. A. Khayer and R. K. Lake, IEEE Electron Device Lett. **30**, 1257 (2009).
[44] M. Luisier and G. Klimeck, J. Appl. Phys. **107**, 084507 (2010).